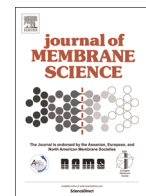




ELSEVIER

Contents lists available at ScienceDirect

## Journal of Membrane Science

journal homepage: [www.elsevier.com/locate/memsci](http://www.elsevier.com/locate/memsci)

## Energy storage by reversible electro dialysis: The concentration battery

Ryan S. Kingsbury<sup>a,b,\*</sup>, Kevin Chu<sup>a,b</sup>, Orlando Coronell<sup>b</sup><sup>a</sup> Bluecell Energy LLC, 2 Davis Drive, Research Triangle Park, NC 27709, USA<sup>b</sup> Department of Environmental Sciences and Engineering, Gillings School of Global Public Health, University of North Carolina at Chapel Hill, Chapel Hill, NC 27599, USA

## ARTICLE INFO

## Article history:

Received 24 March 2015

Received in revised form

29 May 2015

Accepted 27 June 2015

Available online 9 July 2015

## Keywords:

Energy storage

Reverse electro dialysis

Electro dialysis

Ion exchange

Salinity gradient power

## ABSTRACT

Reverse electro dialysis has long been recognized as a tool for harnessing free energy from salinity gradients but has received little attention for its potential in energy storage applications. Here we present the experimental and modeled performance of a rechargeable electro dialytic battery system developed for the purpose of energy storage. Experimental round-trip energy efficiency ranged from 21.2% to 34.0% when cycling the system between 33% and 40–90% state of charge. A mass transport model based on chemical thermodynamics is also proposed to describe the system's performance. Results indicate that, upon model calibration, the model effectively predicts experimental values. Experimental and modeled results suggest that the membrane resistance and osmosis are the primary sources of ohmic and faradaic energy losses, respectively. The results demonstrate that a functioning battery can be constructed using typical reverse electro dialysis stack components. Future improvements in membrane technology and optimization of the system chemistry offer promising avenues to improve the power density, energy density, and round-trip energy efficiency of the process.

© 2015 Elsevier B.V. All rights reserved.

## 1. Introduction

Renewable energy sources such as wind and solar power provide a pathway to a lower-carbon energy future. However, the inconsistent and/or cyclical nature of these supplies limits their value to electric utilities because periods of peak renewable energy output do not necessarily coincide with periods of peak demand for electricity. As such, the ability to store tens or hundreds of MWh of energy is becoming increasingly important to the reliability of electric grids around the world. By storing renewable energy when it is available (e.g. during daytime or periods of strong winds) and releasing it when demand for electricity is the highest, large-scale rechargeable batteries would support the dispatchability of renewable energy supplies as well as the overall stability and reliability of the electric grid. Energy storage technologies will thus play a significant role in modernizing the electrical systems of developed countries and lowering the barriers to electrification for less developed countries or regions. It is predicted that the global demand for large-scale energy storage technologies will exceed 40 GW by 2022 [1].

While numerous technologies exist that are capable of storing

*Abbreviations:* AEM, anion exchange membrane; CEM, cation exchange membrane; ED, electro dialysis or energy density; OCV, open circuit voltage; PD, power density; RED, reverse electro dialysis; SOC, state of charge

\* Corresponding author.

E-mail address: [RyanSKingsbury@alumni.unc.edu](mailto:RyanSKingsbury@alumni.unc.edu) (R.S. Kingsbury).

<http://dx.doi.org/10.1016/j.memsci.2015.06.050>

0376-7388/© 2015 Elsevier B.V. All rights reserved.

such quantities of energy, few have achieved the combination of low capital cost, long operating life, and high round-trip energy efficiency that are required to make a compelling economic case for widespread deployment [2–5]. Battery systems in particular must often employ either rare, expensive, and/or hazardous materials (e.g. lithium, vanadium, lead, sulfuric acid) and/or highly specialized manufacturing techniques, both of which result in high system cost.

In this paper we propose a rechargeable concentration battery which stores energy in the form of an ionic concentration (i.e., chemical potential) difference between two electrolyte solutions. The battery is charged by using electrical energy to perform electro dialysis (ED) on the solutions, creating a concentration difference. The system can later be discharged by reverse electro dialysis (RED), which reconverts the chemical potential energy into direct current electricity. To the authors' knowledge, this paper presents the first experimental results of this type of concentration battery in the peer-reviewed literature.

Electro dialysis (ED) uses direct-current electricity and a stack of alternating anion exchange membranes (AEMs) and cation exchange membranes (CEMs) to move ions from a feed solution to a concentrated solution. ED has been employed for several decades in applications such as desalination of drinking water, food processing, and the treatment of industrial wastes [6,7]. The reverse process (reverse electro dialysis, RED) was proposed in the 1970s as a means of harnessing electrolyte concentration differences in e.g. seawater and river water to produce renewable electricity [8]. In

the last decade, RED has become an active area of research [9–19], but remains challenged by three primary sources of energy loss: the low conductivity of the dilute solution (generally river water), fouling by natural materials in the feed water, and performance limitations of the ion exchange membranes (i.e. high resistance, low selectivity, insufficient power density) [12,14,15,20–22].

As long as a reversible electrode system is used, both ED and RED can be performed using the same apparatus. Several such electrode systems have been described in the literature [23–25]. As such, it is possible to construct a rechargeable battery system that uses ED to charge the battery by converting electrical energy into chemical potential energy in the form of a concentration difference, and RED to discharge the battery by converting said chemical potential energy back into electricity. While there has been some research of closed-loop RED for generating energy from low-grade heat [26–28] (in which the solutions are continuously regenerated by thermal means), the use of a *rechargeable concentration battery* represents a novel approach to the problem of energy storage which may offer several distinct advantages over traditional battery systems.

From a materials standpoint, the electrolyte may be selected from a variety of non-toxic, environmentally benign salts (such as sodium chloride). This flexibility would allow the system to benefit from existing economies of scale in certain electrolytes such as road de-icing salts and well completion fluids. Furthermore, the design is inherently safer than that of a traditional battery since the position of the electrodes within the electrodiolysis stack virtually eliminates the risk of thermal runaway. Finally, the power capacity (membrane area) and the energy capacity (electrolyte volume) can be independently scaled to suit different application requirements; a characteristic currently offered only by redox flow batteries [5].

Given these potential advantages, the first objective of this study was to build and test a laboratory-scale prototype of a rechargeable electrodiolytic concentration battery. The second objective was to develop a mathematical model based on chemical thermodynamics to describe the performance of the system. The

model combines established concepts and equations in electrodiolysis, reverse electrodiolysis, and battery systems. The modeling results provide insight into the relative impact of various design and operating variables on the round-trip energy efficiency, power density, and energy density of the system.

## 2. Formulation of model to describe battery performance

### 2.1. Overview of battery operation and corresponding phenomena to be modeled

At its core, the concentration battery is a closed-loop (reverse) electrodiolysis, (R)ED, system as illustrated in Fig. 1. In the system, an (R)ED stack comprising alternating CEMs and AEMs separates two electrolyte solutions stored in tanks, which may initially be at the same concentration. The solutions are circulated through the (R)ED stack by pumps in a closed loop. Working electrodes at either end of the stack (the battery terminals) allow electricity from a power source to be transferred into the solutions as ionic current. To charge the battery, an electric current is applied to the stack to cause ED, resulting in a net movement of ions out of one of the solutions and into the other. As the charging process continues, a concentration gradient develops between the two solutions, and a chemical potential difference is established across the membrane stack. When the externally-applied electric current through the system is stopped and the circuit is kept open, the system is effectively storing energy as a salinity gradient. When the circuit is closed by connecting it to an electrical load, the chemical potential drives a current in the reverse direction through RED, discharging the system and eventually returning it to the initial state in which both electrolyte concentrations are equal. Thus in theory, a closed-loop (R)ED system can be charged with electrical energy by ED to later discharge the stored energy by RED.

The theoretical energy storage capacity of the system is given by the Gibbs free energy of mixing between the solutions,  $\Delta G_{mix}$ ,

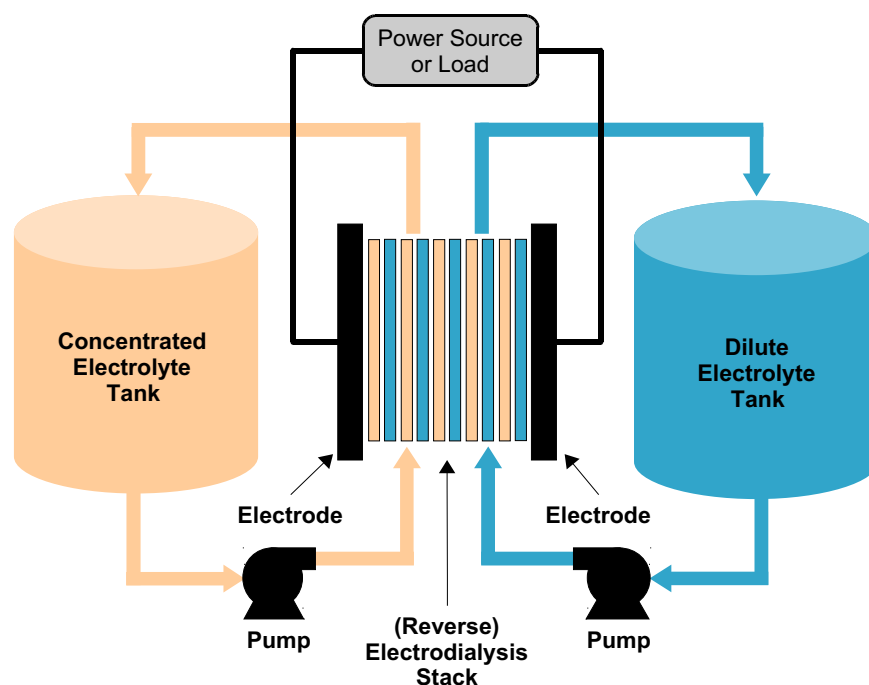


**Fig. 1.** Schematic diagram of closed-loop electrodiolytic energy storage system – the concentration battery. During charging by ED, ions migrate from the dilute to the concentrated electrolyte. When discharging by RED, the direction of electrical current is reversed and ions move back from the concentrated to the dilute electrolyte, eventually restoring the initial concentrations. (See Figs. 2 and 4 for details of the interior of the (reverse) electrodiolysis stack.)

which can be calculated as [9,10,15,29,30]

$$\Delta G_{\text{mix}} = \Delta G_{C,c} + \Delta G_{D,c} - \Delta G_{C,d} - \Delta G_{D,d}, \quad (1)$$

where the upper-case subscripts *C* and *D* refer to the concentrated and dilute solutions, respectively, and the lower-case subscripts *c* and *d* refer to the charged and discharged states, respectively. The Gibbs free energy in each solution is calculated as

$$\Delta G = RT \sum_i n_i \ln a_i, \quad (2)$$

where  $n_i$  is the number of moles of species *i* in solution,  $a_i$  (–) is the activity of species *i* in solution,  $T$  (K) is the absolute temperature, and the constant  $R$  represents the universal gas constant (8.314 J/mol K).

By using the activity in Eq. (2), Eq. (1) accounts for non-ideal solution–solvent interactions. Replacing the activity with the mole fraction  $x_i$  (–) yields

$$\Delta G_{\text{ideal}} = RT \sum_i n_i \ln x_i, \quad (3)$$

which represents the ideal free energy change based on mixing entropy [9,10,15]. Using Eqs. (1)–(3), it is possible to calculate the total amount of energy available from the mixing of two volumes of electrolyte solution.

The electrical characteristics of ED and RED systems (e.g. voltage, resistance, power density) have been modeled extensively. However, since these processes are continuous-flow, they reach a steady-state, which simplifies modeling of mass transport through the membranes and allows some phenomena to be neglected. For example, in RED, water transport by electro-osmosis tends to offset transport by osmosis [16,31]. To model the performance of the closed-loop concentration battery proposed in this work and estimate the electrical characteristics of the system using ED/RED equations, it is necessary to develop a time-dependent model that accounts for all processes that move ions or water from the concentrated to the dilute solution (or vice versa). These calculations must be carried out for a discrete time step and integrated over an entire charging or discharging stage to be meaningful. The remainder of this section formulates such a model.

## 2.2. State of charge of the concentration battery

The state of charge (SOC) of a battery system is related to how much of its chemical energy is available for discharge. For the concentration battery, we propose a definition for SOC based on how the transportable ions are distributed between the concentrated and dilute solutions. At 100% charge, all of the transportable ions are in the concentrated solution, while at 0% charge, the ions are evenly distributed between the two solutions (i.e. the concentrations are equal). Using this frame of reference, the state of charge can be expressed as

$$\text{SOC} = \frac{\sum_i C_{C,i} - \sum_i C_{D,i}}{\sum_i C_{C,i} + \sum_i C_{D,i}}, \quad (4)$$

where  $C_{C,i}$  and  $C_{D,i}$  represent the concentration (mol/L) of species *i* in the concentrated and dilute solutions, respectively, and the summation extends over all the ions that can move through the membrane. Note that changes in the relative volumes of the solutions due to the addition or subtraction of water (e.g. by osmosis) are implicitly accounted for in the concentration terms, but that the SOC does not depend on the absolute volumes of the solutions. In a practical system, it is unlikely that 100% charge would ever be reached; the resulting extreme concentration gradient would cause enough back-diffusion of salt into the dilute compartment that some residual ions would always be present.

## 2.3. Electrical characteristics of the concentration battery: voltage and resistance

Given a certain SOC, the electrical characteristics of the concentration battery can be calculated using familiar equations from ED/RED. The open circuit voltage developed in an (R)ED apparatus that separates two electrolyte solutions of different concentration is determined by the membrane potentials (i.e., the potentials across each individual AEM or CEM). Membrane potentials are the result of Donnan potentials arising from the discontinuity in the ion concentration at each membrane interface, and diffusion potentials arising from the dissimilar mobility of anions and cations inside the membrane phase [31–34]. The membrane potential ( $\psi_{\text{mem}}$ , volts), Donnan potential ( $\psi_{\text{Don}}$ , volts) and diffusion potential ( $\psi_{\text{diff}}$ , volts) for any given membrane are expressed by [31–34]:

$$\psi_{\text{mem}} = \psi_{\text{Don}1} + \psi_{\text{diff}} - \psi_{\text{Don}2}, \quad (5)$$

$$\psi_{\text{Don}} = -\frac{RT}{z_i F} \ln \frac{\bar{a}_i}{a_i}, \quad (6)$$

and

$$\psi_{\text{diff}} = -\frac{RT}{F} \int_{\bar{a}_{i,1}}^{\bar{a}_{i,2}} \sum_i \frac{\bar{t}_i}{z_i} d \ln \bar{a}_i, \quad (7)$$

respectively, where subscripts 1 and 2 indicate the two membrane–solution interfaces (i.e., interfaces with the concentrate and dilute solutions), subscript *i* represents either the co-ion or counter-ion (in Eq. (6)) or all ionic species (in Eq. (7)),  $\bar{t}_i$  (mol/mol charge) is the membrane phase transport number [31],  $z_i$  (–) is the formal charge of species *i*, and  $a_i$  (–) and  $\bar{a}_i$  (–) are the activities of species *i* in the bulk solution and the membrane phase, respectively. The constant  $F$  represents the Faraday constant (96,485 C/mol).

The membrane-phase transport number ( $\bar{t}_i$ , mol ions/mol charge) represents the fraction of the total applied electrical current carried by species *i*, and can be calculated in a manner analogous to the transport number in the free solution as [31]

$$\bar{t}_i = \frac{\bar{D}_i z_i^2 \bar{C}_i}{\sum_i \bar{D}_i z_i^2 \bar{C}_i}, \quad (8)$$

where  $\bar{D}_i$  (m<sup>2</sup>/s) and  $\bar{C}_i$  (mol/L) are the diffusion coefficient and concentration of species *i*, respectively, in the membrane phase.

If the transport number is considered constant throughout the membrane phase, the integration in Eq. (7) can be neglected [31]. Accordingly, in this work, the transport number was assigned a constant value equal to the average of the transport numbers at each interface, which allows Eq. (7) to be re-written as

$$\psi_{\text{diff}} = -\frac{RT}{F} \sum_i \frac{\bar{t}_{i,C} + \bar{t}_{i,D}}{2z_i} \ln \frac{\bar{a}_{i,C}}{\bar{a}_{i,D}}, \quad (9)$$

where the subscripts *C* and *D* refer to the interface with the concentrated and dilute solutions, respectively. The constant transport-number assumption is reasonable when the bulk solution concentrations at the two interfaces are relatively similar [31], as is the case in this work.

Using Eqs. (5), (6) and (9) to determine the membrane potential across individual AEMs and CEMs, the open-circuit voltage of the entire stack ( $E_{\text{OCV}}$ ) can be calculated by multiplying the potential of an AEM–CEM membrane pair by the number of membrane pairs ( $N$ , –) as given by

$$E_{\text{OCV}} = N(\psi_{\text{mem,AEM}} + \psi_{\text{mem,CEM}}). \quad (10)$$

A careful analysis of Eqs. (6), (7), (9) and (10) indicates that there is a unique relationship between the  $E_{\text{OCV}}$  and the ionic

concentrations in the concentrated and dilute solutions. Given that Eq. (4) also indicates a unique relationship between the SOC and the ionic concentrations in the concentrated and dilute solutions, then there is also a unique correspondence between the SOC and the  $E_{OCV}$ . In practical terms, the  $E_{OCV}$  can be used to indicate the state of charge of the battery.

The total battery voltage across its terminals ( $E$ , volts), when current is flowing is found by adding the open circuit voltage to the voltage drop due to the membrane stack resistance (i.e. the battery's resistance) as given by Ohm's law:

$$E = E_{OCV} \pm IR_{stack}, \quad (11)$$

where  $I$  (Amp) is the current passing through the battery, and  $R_{stack}$  (ohm) is the overall resistance of the membrane stack. During the charging stage, the ohmic losses add to  $E_{OCV}$ , while during discharging, ohmic losses are subtracted, thus reducing the total battery voltage.

The three primary sources of  $R_{stack}$  are the solutions, membranes, and electrodes. The  $R_{stack}$  can be calculated according to [9]

$$R_{stack} = \frac{N}{A} \left( \frac{r_{AEM}}{1-\beta} + \frac{r_{CEM}}{1-\beta} + \frac{\delta_C}{\epsilon^2 \kappa_C} + \frac{\delta_D}{\epsilon^2 \kappa_D} \right) + R_{electrode}, \quad (12)$$

where  $A$  ( $m^2$ ) is the area of each membrane in the stack,  $r_{AEM}$  ( $\Omega m^2$ ) and  $r_{CEM}$  ( $\Omega m^2$ ) are the areal resistances of each AEM and CEM, respectively,  $\beta$  (-) is the fraction of membrane area that is covered by the spacer (termed the spacer shadow factor [13]),  $\kappa_C$  (S/m) and  $\kappa_D$  (S/m) are the specific conductivities of the concentrated and dilute solutions, respectively,  $\delta_C$  (m) and  $\delta_D$  (m) are the thicknesses of the concentrated and dilute flow channels, respectively (i.e., the spacing between membranes),  $\epsilon$  (-) is the porosity of the spacer material, and  $R_{electrode}$  ( $\Omega$ ) is the total resistance of the electrode system. In a full-scale system with hundreds of membranes,  $R_{electrode}$  is negligible compared to the other components [9,13,15], but at laboratory scale it can be much more significant.

#### 2.4. Battery performance: round-trip energy efficiency, power density, and energy density

The three main performance characteristics of interest for a battery system are the round-trip energy efficiency, power density, and energy density. The round-trip energy efficiency reflects the losses associated with charging and discharging the system. Power density measures the amount of electrical power that can be produced by each unit of membrane area, and has a significant impact on the capital cost of the system (due to the relatively high cost of ion exchange membranes). Energy density is a measure of the physical size of the system that would be required to store a given quantity of energy.

The round-trip energy efficiency ( $\eta$ , -) is defined as the ratio of the energy released during discharge to the energy required to charge the battery back to the initial charged state. Energy efficiency can be represented as the product of a current efficiency  $\eta_i$  (-) and a voltage efficiency  $\eta_V$  (-) as given by [35]

$$\eta = \eta_V \eta_i = \frac{\int_0^{t_d} I_d E_d dt}{\int_0^{t_c} I_c E_c dt}, \quad (13)$$

$$\eta_i = \frac{\int_0^{t_d} I_d dt}{\int_0^{t_c} I_c dt}, \quad (14)$$

and

$$\eta_V = \frac{\frac{1}{t_d} \int_0^{t_d} E_d dt}{\frac{1}{t_c} \int_0^{t_c} E_c dt}. \quad (15)$$

In Eqs. (13)–(15),  $t$  (s) is the duration of charge or discharge, and subscripts  $c$  and  $d$  denote charging and discharging stages, respectively. To measure a meaningful round-trip energy efficiency, the charge–discharge test must begin and end at the same state of charge, which is indicated by  $E_{OCV}$ , as discussed in the previous section.

The current efficiency is a measure of the fraction of charge used to charge the battery that is available for useful work during the discharge process; low current efficiencies indicate significant faradaic losses – “leaks” of electrical charge due to self-discharge phenomena. The voltage efficiency can be interpreted as the ratio of the average voltage (i.e. the energy available per unit current) during discharging over that during charging; low voltage efficiencies indicate high losses and therefore high internal resistance.

Power density ( $PD$ ,  $W/m^2$ ) is defined as the power output available during discharge per total membrane area:

$$PD = \frac{I_d E_d}{2NA} = \frac{j E_d}{2N}, \quad (16)$$

where  $j$  ( $A/m^2$ ) is the current density, representing the current normalized to membrane area. While in RED systems, the power output is constant due to constant feed water concentrations, in the concentration battery, the power output is continuously changing. When the battery starts to discharge, the concentration difference is at its highest, and the battery voltage ( $E_d$ ) is correspondingly high. As the ionic concentration difference between concentrated and dilute solutions decreases, the battery voltage and the power output drop. As such, for energy storage, the relevant parameter is the average power density throughout the discharge stage which can be calculated as

$$PD_{avg} = \frac{1}{t_d} \int_0^{t_d} \frac{j E_d}{2N} dt. \quad (17)$$

The energy density ( $ED$ ,  $J/m^3$ ) can be calculated by dividing the total discharged energy by the total concentrated and dilute solution volumes as given by

$$ED = \frac{\int_0^{t_d} E_d I_d dt}{(V_C + V_D)}, \quad (18)$$

where  $V$  ( $m^3$ ) represents volume.

#### 2.5. Mass transport processes in the concentration battery

The equations presented thus far allow for the calculation of the electrical properties of the concentration battery when the state of the battery (concentrations, activities, etc.) is known. During operation, however, the electrolyte concentrations are constantly changing due to (reverse) electro dialysis between the concentrated and dilute compartments. Therefore, it is necessary to describe the mass transport between the two compartments in order to model the overall performance of the concentration battery.

Because the concentration battery is a closed system, the mass balance on a given species  $i$  in either the dilute or concentrated solution is a function only of the flux through the membrane surfaces as given by

$$n_i = n_{i,0} \pm 2N(1-\beta)A \int_0^t (J_{i,AEM} + J_{i,CEM}) dt, \quad (19)$$

where  $n_{i,0}$  is the initial number of moles in the solution of interest and  $J_{i,AEM}$  and  $J_{i,CEM}$  are the fluxes ( $mol/m^2/s$ ) of species  $i$  through

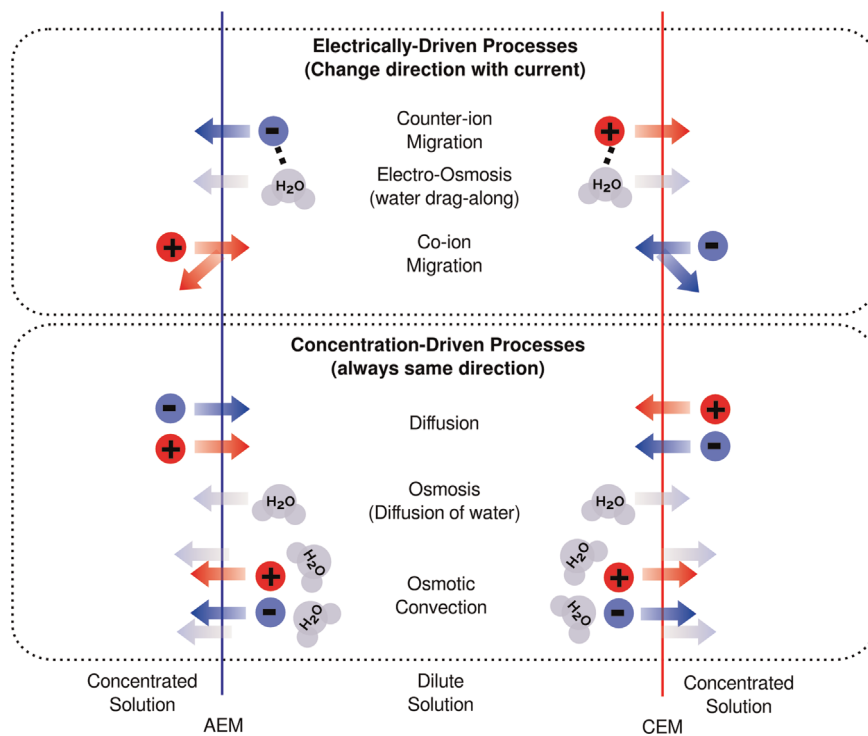


Fig. 2. Mass transport processes occurring in the concentration battery. The top and bottom panels depict electrically-driven and concentration-driven processes, respectively. The direction of transport shown corresponds to that occurring during the battery charging (electrodialysis) stage.

the AEM and CEM, respectively. The sign of the flux is negative and positive for departure and arrival, respectively, of species from/to the solution. For example, for the dilute solution, the flux of ions will be negative during charging (indicating electrodialysis) and positive during discharging (indicating reverse electrodialysis).

Fig. 2 summarizes the mass transport processes occurring in the membrane stack. The top and bottom panels of Fig. 2 depict electrically-driven and concentration-driven processes, respectively. The electrically-driven counter-ion and co-ion migration and electro-osmosis (i.e., the “dragging along” of water molecules by friction as ions move through the membrane) can be reversed by changing the direction of the current. Therefore, the electrically-driven processes occur in opposite directions during the charge (as shown in Fig. 2) and discharge (opposite to Fig. 2) stages. By contrast, the concentration-driven diffusion of ions, osmosis, and osmotic convection always occur down the concentration gradient of the ions (ion diffusion) and water (osmosis and osmotic convection). Therefore, the concentration-driven processes always occur in the directions shown in Fig. 2 for both the charge and discharge stages. Given that the concentration-driven processes tend to discharge the battery, and some of the (electrical) energy used during charging is used to counteract the concentration-driven processes, then the round-trip energy efficiency is always lower than 100%.

The migration flux of counter-ions and co-ions is determined by the corresponding ion transport numbers in the membrane phase (see Eq. (8)) and can be calculated as [6,34]

$$J_{i,migration} = - \frac{j\bar{t}_i}{(1-\beta)z_iF}, \quad (20)$$

where  $J_{i,migration}$  (mol/m<sup>2</sup>/s) represents the migration flux of any given ion  $i$ . The spacer shadow factor term in the denominator is necessary because the local current density at the membrane surface is higher than  $j$  due to the blocking effect of the spacer.

In a similar manner, the electro-osmotic flux of water ( $J_{w,electro-osmosis}$ , mol/m<sup>2</sup>/s) is determined by a water transport

number ( $\bar{t}_w$ , mol H<sub>2</sub>O/mol charge) that represents the moles of water carried along by each mole of ions that is moved by migration [32], and can be calculated as

$$J_{w,electro-osmosis} = - \bar{t}_w \sum_i J_{i,migration}, \quad (21)$$

The water transport number is a membrane property that is determined experimentally (see Section 3). The measured value for a given membrane is typically interpreted as the average water transport number for both ions in the salt solution [32,36].

The diffusive flux of ions is calculated from the gradient in the ion's electrochemical potential between concentrated and dilute solutions as (see Appendix A for derivation)

$$J_{i,diffusion} = - \frac{\bar{D}_i \bar{C}_i \Delta \bar{a}_i}{\bar{a}_i \Delta x}, \quad (22)$$

where  $\Delta \bar{a}_i$  represents the difference in the activity of species  $i$  between the two membrane–solution interfaces and  $\Delta x$  (m) is the membrane thickness.  $\bar{D}_i$ ,  $\bar{C}_i$ , and  $\bar{a}_i$  are taken as averages of the respective values at each interface.

Similarly, the water flux due to osmosis is calculated as

$$J_{w,osmosis} = - \frac{\bar{D}_w \bar{C}_w \Delta \bar{a}_w}{\bar{a}_w \Delta x}, \quad (23)$$

where  $\bar{D}_w$  (m<sup>2</sup>/s),  $\bar{C}_w$  (mol/L) and  $\bar{a}_w$  (–) correspond to the diffusion coefficient, average concentration and average activity, respectively, of water in the membrane phase.

Finally, the movement of water through the membrane by osmosis creates a bulk convection velocity that carries ions along with it, resulting in a flux of ions from the dilute solution into the concentrated solution. This osmotic convection was accounted for by multiplying the bulk solution concentration of the ion by the osmotic flux as given by

$$J_{i,convection} = J_{w,osmosis} C_{D,i} V_w^m, \quad (24)$$

where  $V_w^m$  is the molar volume of water,  $1.82 \times 10^{-5}$  m<sup>3</sup>/mol, and

$C_{D,i}$  is the concentration of species  $i$  in the bulk dilute solution.

### 2.6. Activity, concentration and diffusion coefficient of ions in the membrane phase

In order to use Eqs. (19)–(24) to describe mass transport through the membrane, it is necessary to determine the concentration, activity, and diffusion coefficient of each ionic species in the membrane phase. The activity of the ions in the membrane phase is related to their activity in the bulk solution through the Donnan equilibrium as given by [33,37]

$$\left(\frac{a_-}{\bar{a}_-}\right)^{\frac{1}{z_-}} \left(\frac{\bar{a}_+}{a_+}\right)^{\frac{1}{z_+}} = \exp\left(\frac{\Delta\pi \bar{V}_s^m}{RTz_+\nu_+}\right), \quad (25)$$

where subscripts  $+$  and  $-$  indicate the cation and anion, respectively, of the parent salt,  $\nu$  represents the stoichiometric coefficient of the ion in the parent salt,  $\bar{V}_s^m$  represents the partial molar volume of the salt, and  $\Delta\pi$  is the difference in osmotic pressure between the membrane and the solution phase.

In addition, electroneutrality must prevail within the

membrane phase, and therefore

$$\bar{C}_+z_+ + \bar{X} + \bar{C}_-z_- = 0, \quad (26)$$

where  $\bar{X}$  (eq/L, including sign) is the fixed charge concentration in the membrane phase.

By using the Pitzer model, which is well documented elsewhere [38], to calculate activity coefficients in bulk solution, we obtain both the concentration and activity of each species in the membrane using Eqs. (25) and (26).

The membrane-phase diffusion coefficients are calculated from the bulk solution diffusion coefficients. The bulk-solution diffusion coefficients available in the literature are typically reported for infinite dilution conditions, and therefore we correct them for viscosity (a function of salt concentration) through the Stokes–Einstein relation (see Appendix B) [34]. Since the membrane-phase diffusion coefficients of various salts have been shown to generally follow the order of their conductivity in bulk aqueous solution [39], diffusion coefficients in the membrane phase were assumed to be proportional to diffusion coefficients in the solution phase as expressed by [6]

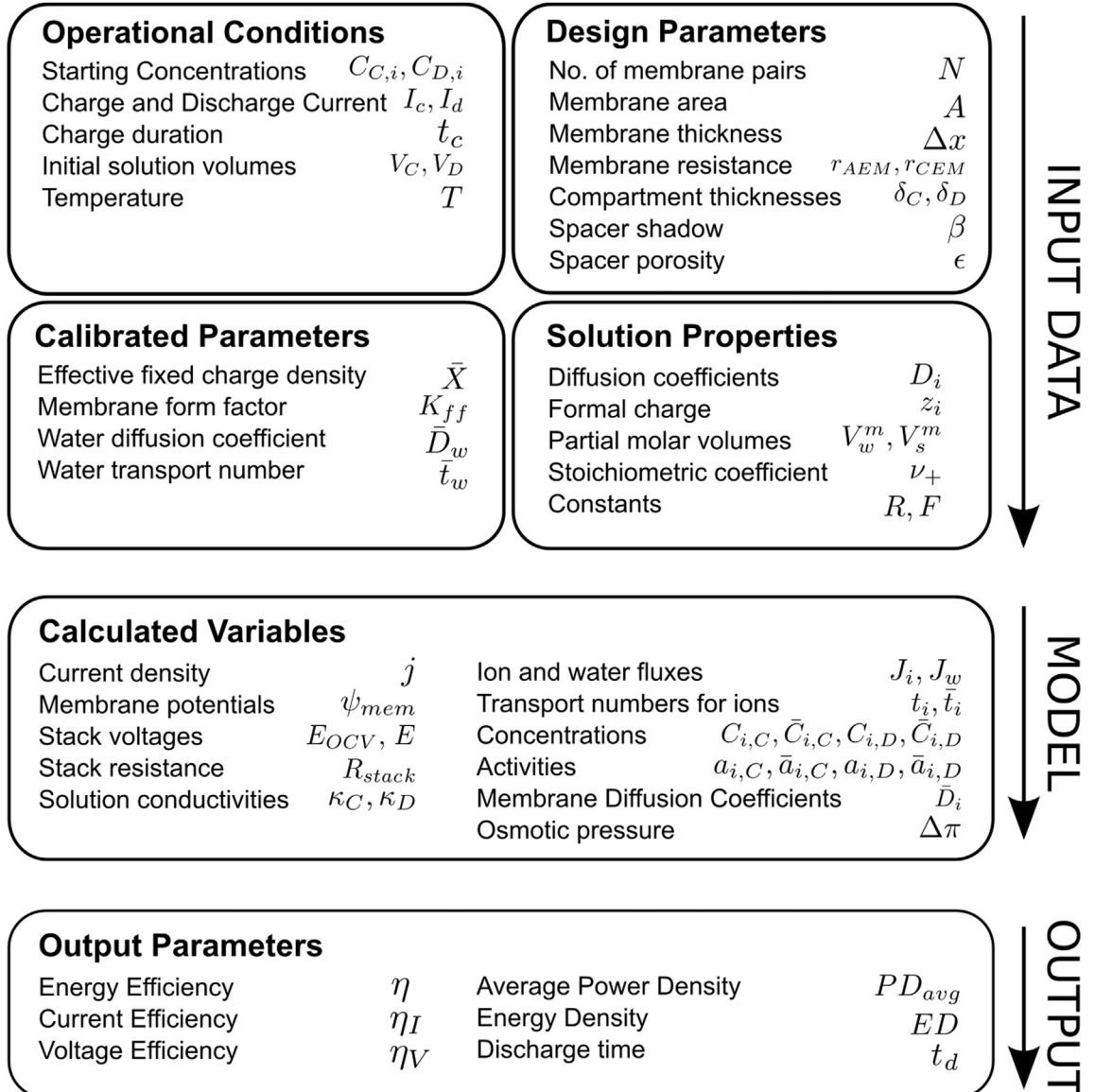


Fig. 3. Overview of input and output variables in the model used to describe the performance of the concentration battery.

$$\bar{D}_i = K_{ff} D_i, \quad (27)$$

where  $K_{ff}$  is a “form factor” [6] specific to each membrane, and common to all ions, that serves as an adjustable parameter during model calibration.

By combining Eqs. (27) and (8), the transport number in the membrane phase can be re-written in terms of the bulk solution diffusion coefficients and calculated membrane phase concentrations as

$$\bar{t}_i = \frac{K_{ff} D_i z_i^2 \bar{C}_i}{K_{ff} \sum_i D_i z_i^2 \bar{C}_i} = \frac{D_i z_i^2 \bar{C}_i}{\sum_i D_i z_i^2 \bar{C}_i}. \quad (28)$$

## 2.7. Model application

The equations presented in Sections 2.1–2.6 comprise the engineering model used to describe the performance of the concentration battery. A summary of the input and output variables for the model is presented in Fig. 3. As shown in the figure, four parameters ( $\bar{X}$ ,  $K_{ff}$ ,  $\bar{D}_w$ ,  $\bar{t}_w$ ), all related to mass transport through the membrane, must be calibrated by experiment before the model can be used. The remaining input data consists of system design parameters (e.g. physical geometry), starting conditions (e.g. concentrations, charging current, etc.), and solution properties (e.g. diffusion coefficients). With the exception of the four calibrated parameters, all of this input data is easily obtained from the literature, membrane specifications, or the physical design of the stack being modeled. Once the proper information is entered, the engineering model calculates the time-dependent mass-transport and power input or output over the course of a charge-discharge test. The results allow calculation of a variety of system performance parameters including round-trip energy efficiency, power density, energy density, and total flux due to each mass transport process.

The initial conditions for the model correspond to the electrolyte concentrations in the concentrated and dilute solutions (the starting SOC), the current during the charge stage, and the duration of the charging period. Using these initial conditions, the energy required to charge the system over a discrete time step is calculated according to Eqs. (5)–(12). Next, the mass transport of ions and water between the concentrated and dilute solutions during that time is calculated according to Eqs. (19)–(28), from which the concentration of each species in the respective solutions for the next time step are calculated. The calculated new conditions are then used as initial conditions for the next time step until

the charging period is complete. Then, the sign of the current is reversed and the process is repeated for each time step until the SOC of the battery returns to the starting value. Note that in our experiments, the current was the same during the charge and discharge stages in order to approximate a galvanostatic cycling test (see Section 3.5). Power, energy, total flux of ions, and total flux of water are integrated over the entire charge-discharge test and used to compute energy efficiencies (Eqs. (13)–(15)), average power density (Eq. (17)) and energy density (Eq. (18)).

## 3. Materials and methods

### 3.1. Stack configuration

A schematic of the (reverse) electro dialysis stack used in this study is presented in Fig. 4. It contained 13 membrane pairs separated by 127  $\mu\text{m}$  thick silicone gaskets (Specialty Manufacturing Inc., Saginaw, MI). Woven mesh spacer material (Sefar Inc., Buffalo, NY, Nitex 03/200-54) with a spacer shadow factor of 46% (54% open area) and a porosity of 74% was used to keep the membranes separated. The AEM and CEM used were FAS-20 and FKE-20, respectively (FuMA-Tech GmbH, Germany). ABS chambers at each end of the stack contained working electrodes made from graphite plates (GraphiteStore.com #BL001245) connected to titanium wire (McMaster-Carr #89145K28). Current was delivered to the stack through the working electrodes using a DC power supply (Agilent E3617A) operating in constant-current mode. The current was measured independently from the power supply readout using a digital multimeter (Southwire 10030S). The ABS chambers also contained polyethylene Luggin capillaries extending within 1 mm of the outer surface of the membranes. Ag/AgCl reference electrodes (Pine Instrument Co., Grove City, PA) were inserted into the Luggin capillaries to enable battery voltage to be measured using a high-impedance multimeter (Fluke model 87). All measurements of voltage in this work were made using the Luggin capillaries; therefore the impact of e.g. working electrode resistance is not accounted for, for reasons described in Section 2.3.

Thicker CEMs (Neosepta CMX) were installed at each end to separate the working electrode rinse chambers from the interior of the membrane stack. Due to the need to keep the Luggin capillaries open to the atmosphere, the pressure inside the electrode rinse chambers was less than that inside the main stack. This pressure difference was not measured but was estimated to be less than 5 psi; Neosepta membranes were selected due to their thickness (approximately 120  $\mu\text{m}$ ) and reinforced design, which

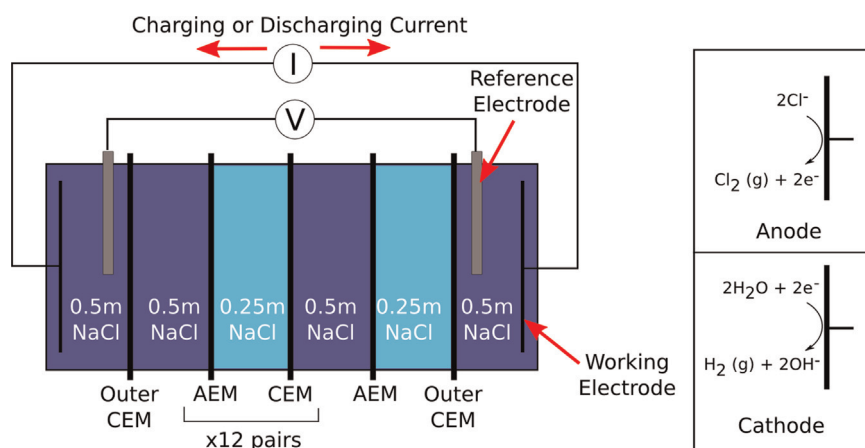


Fig. 4. Schematic representation of the (reverse) electro dialysis apparatus used in this study. The interior CEMs and AEMs were FuMA-Tech FKE-20 and FAS-20, respectively, while the outer CEMs were Neosepta CMX. The inset illustrates reactions occurring at the anode and cathode. Note that each working electrode may serve as the anode or the cathode, depending upon the orientation of the current (charging or discharging).

made them better able to withstand this pressure difference. Therefore, the stack contained a total of 27 membranes including the two outer Neosepta CEMs. The membrane area exposed to the solutions was 35 cm<sup>2</sup> per membrane. Given that the spacer shadow factor was 46% (54% open area) then the effective membrane area was 19 cm<sup>2</sup>.

The dilute and concentrated electrolyte solutions were circulated through their respective chambers in a closed-loop configuration (see Fig. 1) using a dual-head peristaltic pump (Masterflex). Flow rates were adjusted to achieve an interstitial velocity of 2–4 cm/s through the mesh openings. This target velocity range was chosen to minimize boundary layer resistance [13,40]. A separate electrode rinse solution, identical to the concentrated solution, was circulated through both electrode rinse chambers, filling the Luggin capillaries to an adequate height. At the anode, chloride ions were oxidized to chlorine gas, while at the cathode, water was reduced to hydrogen gas. Current transfer was thus accomplished by electrolysis of saltwater at each working electrode. Approximately 15 mmol of sodium formate were added to the electrode rinse solution to stabilize the pH and neutralize aqueous chlorine (HOCl) that may have been generated at the anode by oxidation of chloride ions. This electrode system was employed for experimental convenience; in a full-scale apparatus it would be desirable to use a soluble redox couple that would not result in gas formation at the electrodes.

### 3.2. Determination of the stack resistance

The overall resistance of the membrane stack was determined by setting the power supply to constant-current mode and manually sweeping the current between 0.3 and 1.5 mA/cm<sup>2</sup> in five steps, while the voltage drop across the stack was recorded. The stack resistance was determined from the slope of the current–voltage curve.

### 3.3. Determination of membrane permselectivity

The membrane permselectivity ( $\alpha$ , –) represents the deviation of real ion exchange membrane behavior from that of a perfect membrane in terms of their ability to reject co-ions. An ideal ion exchange membrane completely rejects co-ions, a real membrane does not. Permselectivity was measured at 19 °C by installing a single membrane into the cell and circulating the concentrated (0.5 mol/kg, abbreviated “0.5m” NaCl) and dilute (0.25 mol/kg NaCl) solutions for 30 min to allow the membrane to equilibrate with the concentration difference. After 30 min, 500 mL of fresh solutions were pumped through the concentrated and dilute compartments without recirculation to ensure that the intended concentration difference was maintained. The potential ( $E_{\text{measured}}$ , mV) across the membrane was monitored until a stable value was observed. The potential difference offset ( $E_{\text{offset}}$ , mV) between the two reference electrodes, calculated as the average of the potentials measured by the two electrodes in concentrated solution and in dilute solution, was subtracted from the measured potential to obtain the corrected potential across the membrane ( $E_{\text{corrected}} = E_{\text{measured}} - E_{\text{offset}}$ ) [41]. The  $E_{\text{corrected}}$  was compared to the activity-corrected theoretical open circuit voltage ( $E_{\text{theoretical}}$ , mV) by calculating the ratio between the two as given by [41]

$$\alpha = \frac{E_{\text{measured}} - E_{\text{offset}}}{E_{\text{theoretical}}} \quad (29)$$

$E_{\text{theoretical}}$  was calculated from Eqs. (5)–(7) under the assumption of an ideal membrane (e.g. transport number of the counter-ion = 1), which is equivalent to the familiar Nernst equation [8,21]

$$E_{\text{theoretical}} = \frac{RT}{zF} \ln \frac{a_c}{a_d}, \quad (30)$$

where  $a_c$  and  $a_d$  are the average activity of the salt (NaCl) in the bulk concentrated and dilute solutions, respectively.  $E_{\text{theoretical}}$  was estimated to be 16.2 mV under the conditions tested (0.5 mol/kg and 0.25 mol/kg concentrate and dilute solutions, respectively, at 19 °C). The measured permselectivity was used to calibrate the fixed charge density  $\bar{X}$  in the engineering model (see Section 3.6).

### 3.4. Measurement of self-discharge rate

When the electrolyte solutions are circulated through the concentration battery but no current is applied, the stack voltage  $E$  decreases over time (i.e., self-discharges) due to mass transport by ion diffusion, osmosis, etc. (see Fig. 2). To quantify the rate of self-discharge, 300 mL of fresh concentrated and dilute solutions were circulated through the fully-assembled stack with the working electrodes disconnected (zero current). The stack  $E_{\text{OCV}}$  and the volumes of the concentrated, dilute, and electrode rinse solutions were monitored over a period of 60 min. This measurement yielded the electrical rate of self-discharge (mV/min) and the rate of volume change by osmosis (mL/min), which were needed to calibrate the engineering model (see Section 3.6).

### 3.5. Measurement of battery efficiency

Round-trip energy, current and voltage efficiency was determined through charge–discharge tests beginning with the system in a SOC of 33% using NaCl solutions with concentrations of 0.5 mol/kg and 0.25 mol/kg in the concentrated and dilute compartments, respectively. This starting state was chosen because at lower concentration gradients, the open-circuit voltage of the system is too low to enable efficient energy storage given the magnitude of the stack resistance.

The system was charged and discharged at a constant current to approximate galvanostatic cycling tests conducted on other large-scale battery systems [42]. To start the tests, the open-circuit voltage of the system was measured. Then, a current was applied to the system to initiate the charge of the battery, while the voltage across the stack was recorded using the averaging function of the multimeter, which divides the integrated voltage by the duration of the time step. The charging process was continued for 120 min, and every 15 min, the current, average voltage, concentrated solution volume, and dilute solution volume were recorded. Next, the current was interrupted and the open-circuit voltage of the system was recorded, then charging was resumed. After the charging process was complete, the stack resistance was measured, the current direction was reversed and the system was discharged while following the same procedures. The discharge process continued until the open circuit voltage of the system returned to the starting value. The current, voltage, and round-trip energy efficiencies were calculated as described in Section 2 (see Eqs. (13)–(15)). Note that the efficiency values measured in this way do not account for energy losses due to the resistance of the working electrode chambers and to pumping. In a full-scale system with hundreds of membranes, the resistance of the working electrodes would be negligible compared to the membrane stack resistance [9,13,15]. Pumping losses were estimated by assuming laminar flow through the intermembrane spaces [18,43] and found to have a relatively minor impact on the round-trip energy efficiency, as discussed in Section 4.6.

### 3.6. Model calibration procedure

The measured permselectivity, electrical self-discharge rate,

rate of volume change by osmosis, and stack resistance were used to calibrate the engineering model. The parameters calibrated were the fixed charge concentration ( $\bar{X}$ ) in the CEMs and AEMs, membrane-phase water diffusion coefficient ( $\bar{D}_w$ ) and water transport number ( $\bar{t}_w$ ), membrane form factor ( $K_{ff}$ ), and additional resistance due to the extra CEM and solution in the electrode rinse compartments. First, the fixed charge concentrations ( $\bar{X}$ , eq/L) of the cation exchange and anion exchange membranes were calibrated based on permselectivity data. In the model, the fixed charge concentration determines the membrane phase concentrations (Eqs. (25) and (26)), which in turn determine the transport numbers (Eq. (8)) and ultimately the membrane potential (Eqs. (5)–(7)). As such, the fixed charged concentration for each of the cation and anion exchange membranes was adjusted until the modeled membrane potential for 0.5 mol/kg and 0.25 mol/kg NaCl concentrated and dilute solutions, respectively, matched the experimentally-determined potential from the permselectivity tests described in Section 3.2.

Second, observed rates of volume change (mL/min) during the self-discharge tests and the charge–discharge tests at different current densities were used to calibrate the diffusion coefficient of water ( $\bar{D}_w$ , see Eq. (23)) and water transport number ( $\bar{t}_w$ , see Eq. (21)) for the FuMA-Tech FAS/FKE membrane pair. The rates of volume change were converted to units of flux using the molar volume of water (18.2 cm<sup>3</sup>/mol) and the total membrane area, then plotted against the current density (zero for the self-discharge tests). The intercept with the y-axis (i.e., at zero current density) of the resulting regression line was interpreted as the rate of osmosis (mmol H<sub>2</sub>O/m<sup>2</sup>/s) occurring over the entire membrane stack.  $\bar{D}_w$  was adjusted until the engineering model of the stack produced an equal rate of osmosis.

The slope of the regression line (mmol/s/A) indicated the amount of electro-osmosis that took place. This slope was converted to units of mol H<sub>2</sub>O/mol charge using the Faraday constant, yielding the observed water transport number,  $\bar{t}_w$ .

Third, the electrical self-discharge rate (mV/min) was used to calibrate the membrane form factor ( $K_{ff}$ ) for ion diffusion through the membranes (see Eq. (27)). Apart from osmosis (and the corresponding osmotic convection) already calibrated above, the only other mass transport mechanism active at zero current is ion diffusion. The  $K_{ff}$  parameter sets the membrane-phase diffusion coefficients for the ions, and therefore their rate of diffusion. Thus,  $K_{ff}$  was adjusted until the modeled self-discharge rate (mV/min) at zero current matched the experimental value from the self-discharge test. The self-discharge rate was modeled as described in Section 2.7 for the discharge stage, but in this case no current was applied.

The above steps generated the minimum calibration data necessary to run the model. However, additional calibration of the battery resistance was performed in order to improve the accuracy of the results. The modeled battery resistance calculated by Eq. (12) does not account for the resistance of the extra (Neosepta) CEM (see Fig. 4) or the solution between the tips of the Luggin capillaries and the surface of the outer CEMs (total distance of approximately 1 mm), leading to an underestimation of the real battery resistance of approximately 0.8 Ω. This extra resistance was measured as 0.2 Ω using a stack containing only a single Neosepta CEM. The remaining 0.6-Ω discrepancy can be interpreted as boundary layer resistance, which is also not accounted for in Eq. (12) [40]. An additional 0.8-Ω term (similar to  $R_{electrode}$ ) was added to Eq. (12) in order to capture these effects and calibrate the modeled battery resistance to the measured value.

**Table 1**

Membrane properties for the anion exchange membrane (FAS-20) and cation exchange membrane (FKE-20) used in battery performance tests.

	FAS-20 (AEM)	FKE-20 (CEM)
<b>Reference properties (from specifications)</b>		
Ion exchange capacity (IEC) (meq/g dry membrane) [44,45]	1.86	1.29
Area Resistance (Ω cm <sup>2</sup> ) [44,45]	0.54	0.71
Permselectivity in 0.5 mol/L/0.1 mol/L KCl [44,45]	94%	> 99%
Swelling degree (SD) (g H <sub>2</sub> O/g dry membrane) [44,45]	7	15
Fixed charge concentration (eq/L) <sup>a</sup>	26.6	−8.6
Thickness (μm) [44,45]	20	20
<b>Measured properties</b>		
Permselectivity in 0.5m/0.25m NaCl <sup>b,c</sup>	81.3 ± 2%	99.6 ± 3%
Water transport number (mol H <sub>2</sub> O/mol charge)		13.9
<b>Calibrated model parameters</b>		
Effective fixed charge concentration (eq/L) <sup>d</sup>	0.81	−8.2
Permselectivity in 0.5m/0.25m NaCl	81.4%	99.6%
Membrane Form Factor		0.0028
Water diffusion coefficient (m <sup>2</sup> /s)		4.98e−10

<sup>a</sup> Calculated as IEC/SD\*100 [18].

<sup>b</sup> Values and uncertainties represent the average and standard deviation, respectively, of three replicates.

<sup>c</sup> “m” denotes mol/kg units.

<sup>d</sup> Assuming ideal Donnan exclusion. See Eq. (24).

## 4. Results and discussion

### 4.1. Calibration of membrane properties

Table 1 summarizes expected, measured and calibrated membrane properties. The measured permselectivity of the AEM (81.3%) was significantly lower than expected based on the specified value (94%). It is unclear whether this result is related to the different measurement conditions (0.5 mol/kg/0.25 mol/kg NaCl in our tests versus 0.5 mol/L/0.1 mol/L NaCl used in specifications) or some other factor. Similar results were obtained when conducting

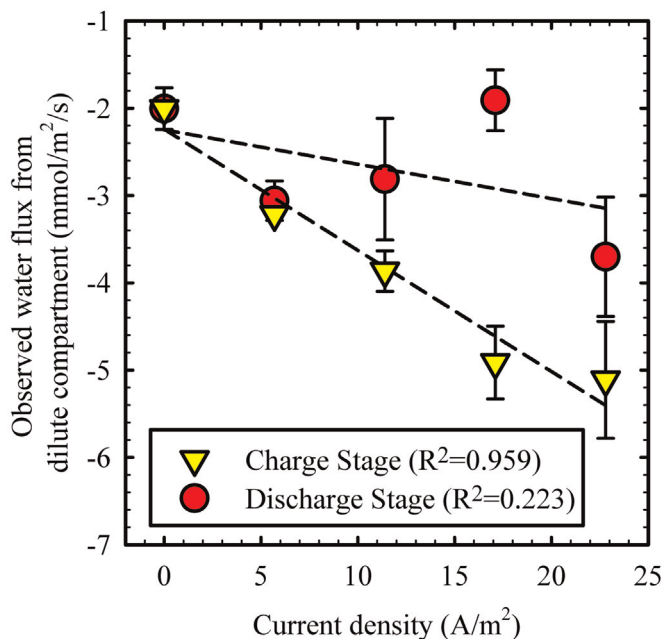


**Fig. 5.** Observed rate of osmosis and electro-osmosis during charging and discharging. Data points and error bars correspond to the average and standard deviation of two replicates, respectively. At zero current density, the data show the average and standard deviation of three replicates, and these replicates are common to both the charge and discharge stages.

a preliminary measurement on a Neosepta AMX membrane however, so the low permselectivity under these conditions does not appear to be specific to one type of AEM. It is possible that Donnan exclusion is not very effective within the polymer matrix as a result of water uptake by the polymer or the elevated concentration on the dilute side of the membrane [41]. As such, the calibrated fixed charge concentration for the AEM (0.81 eq/L) was significantly lower than would be expected based on the specified ion exchange capacity (IEC) and swelling degree (SD) [44,45]. The permselectivity (99.6%) and calibrated fixed charge concentration ( $-8.2$  eq/L) for the CEM were both very close to the corresponding membrane specifications ( $> 99\%$  and  $-8.6$  eq/L, respectively). See Appendix C for raw measurement data.

Fig. 5 shows observed rates of water flux from the dilute solution during both self-discharge tests at zero current and charge-discharge tests. The rates of water flux during the charging stage (ED) exhibit a clear linear relationship to the current, while those during discharging stage (RED) have a less clear relationship to current. Using the slope of the charging line yields an estimated water transport number of  $13.9$  mol  $H_2O$ /mol charge, which was used in Eq. (21) to calculate electro-osmosis. This value is in reasonable agreement with the value of  $11.7$  mol  $H_2O$ /mol charge reported by Veerman et al. [16] for the similar FAD/FKD membrane pair. In general, water transport numbers within ion exchange membranes have been reported to range from approximately  $2$ – $12$  mol/mol [16,36], placing the value for this membrane pair at the upper end of the expected range.

The intercept of the electro-osmosis regression lines provided the basis for calibrating the water diffusion coefficient  $\bar{D}_w$  used in Eq. (23). The calibrated value of  $4.98 \times 10^{-10}$   $m^2/s$  is comparable to some representative values for other membranes reported by Veerman et al., which ranged from  $5.8 \times 10^{-11}$  to  $1.2 \times 10^{-9}$   $m^2/s$  [16].

After calibration of the water diffusion coefficient, the membrane form factor  $K_{ff}$  was fitted to match the modeled self-discharge rate (mV/min) to the observed self-discharge rate of  $0.66 \pm 0.16$  mV/min. The fitted  $K_{ff}$  value was  $0.0028$ .

#### 4.2. Battery efficiency

Table 2 presents experimental battery efficiencies alongside simulation results. With a constant charging time of  $120$  min at current densities between  $5.7$  and  $22.8$   $A/m^2$ , the experimental round-trip energy efficiency ranged from  $21.2\%$  to  $34.0\%$ .

As shown in Table 2, the discharge times are all less than  $120$  min, resulting in current efficiency lower than  $100\%$  (see Eq. (14)). Self-discharge phenomena such as counter- and co-ion diffusion, co-ion migration, and osmosis are responsible for these reductions in current efficiency. The current efficiency ranged from  $27.1\%$  to  $58.9\%$  and showed a clear increasing trend with current density, while the voltage efficiency ranged from  $52.6\%$  to  $78.5\%$  and decreased in a nearly linear fashion with current density, as shown in Fig. 6. These relationships can be explained by the interplay between ohmic and faradaic energy losses. At low current densities, the ohmic losses due to internal resistance are small, but the rate of self-discharge by diffusion and osmosis is nearly equal to the charging current, resulting in low current efficiency and little energy storage (low round-trip energy efficiency). At higher currents, the rate of charging is much greater than the rate of faradaic loss to self-discharge, but the higher ohmic losses reduce the total voltage across the stack (see Eq. (11)), leading to a low voltage efficiency. The optimum current density occurs where the collective energy losses from these two sources are minimized, which appears to correspond to a current density between  $11$  and  $17$   $A/m^2$ .

Both the  $E_{OCV}$  and stack resistance in the charged state increased with increasing current density, as shown in Table 2. This

**Table 2** Experimental and simulated battery efficiency results with a charging time of  $120$  min. Uncertainties indicate the standard deviation of two replicates; uncertainties for the starting conditions indicate the standard deviation of all tests (eight replicates).<sup>a</sup>

Current density $A/m^2$	Round-trip energy efficiency %	Current efficiency %	Voltage efficiency %	Obtained state of charge %	Obtained $E_{OCV}$ mV	Resistance when charged $\Omega$	Discharge time min	Final concentrate volume mL	Final dilute volume mL	Average power density $W/m^2$	Energy density mWh/L
Starting condition <sup>b</sup>	–	–	–	(33.0)	$374 \pm 11$	$2.3 \pm 0.1$	–	$297 \pm 6$	$301 \pm 6$	–	–
5.7	$21.2 \pm 2.2$ (23.3)	$27.1 \pm 3.0$ (29.2)	$78.5 \pm 0.1$ (80.0)	(39.7)	$461 \pm 8$ (462)	$2.3 \pm 0.1$ (2.3)	$32.5 \pm 3.5$ (35)	$343 \pm 11$	$250 \pm 0$	$0.07 \pm 0.001$ (0.08)	$7 \pm 1$ (7)
11.4	$34.0 \pm 1.3$ (33.7)	$48.8 \pm 1.8$ (49.2)	$69.7 \pm 0.3$ (68.5)	(53.8)	$713 \pm 18$ (663)	$2.5 \pm 0.2$ (2.5)	$58.5 \pm 2.1$ (59)	$325 \pm 21$	$238 \pm 4$	$0.18 \pm 0.01$ (0.18)	$29 \pm 3$ (27)
17.1	$34.0 \pm 1.2$ (35.1)	$56.3 \pm 3.0$ (56.7)	$60.4 \pm 1.0$ (61.9)	(70.3)	$1074 \pm 64$ (967)	$3.5 \pm 0.2$ (2.8)	$67.5 \pm 3.5$ (68)	$350 \pm 28$	$235 \pm 7$	$0.33 \pm 0.02$ (0.31)	$59 \pm 2$ (54)
22.8	$30.9 \pm 0.4$ (34.9)	$58.9 \pm 5.1$ (60.0)	$52.6 \pm 3.8$ (58.2)	(90.5)	$1729 \pm 211$ (1688)	$11.9 \pm 0.5$ (4.7)	$66.5 \pm 12.0$ <sup>b</sup> (72)	$263 \pm 138$ <sup>b</sup>	$200 \pm 0$	$0.44 \pm 0.02$ (0.52)	$87 \pm 14$ (95)

<sup>a</sup> Simulation results appear in parentheses. Initial concentrated and dilute solutions of  $0.5$  and  $0.25$  mol/kg NaCl, respectively, were used. Average temperature during all tests was  $18.5 \pm 1.3$  °C.

<sup>b</sup> Charging was halted at  $105$  min during one test because the stack appeared to reach limiting current density. A leak developed from the concentrate compartment during the test, causing the system to charge more rapidly than usual. Hence, the discharge time and final concentrate volume for one test was much lower than the other.

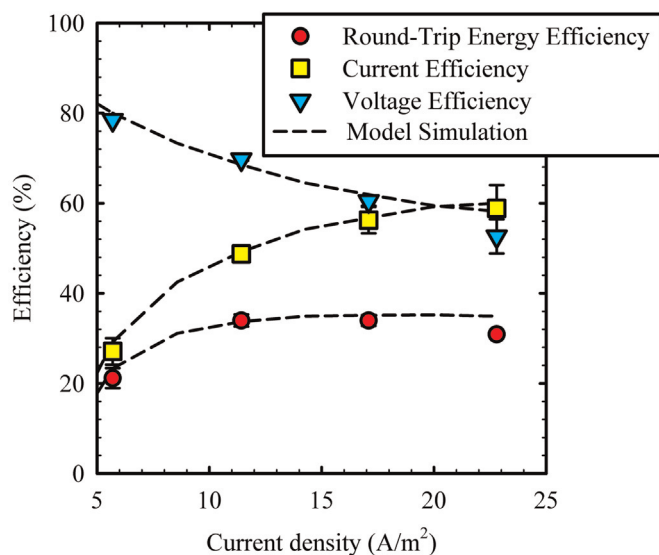


Fig. 6. Experimental and simulated battery efficiency results. Data points and error bars correspond to the average and standard deviation of two replicates, respectively.

is consistent with mass transport expectations by electro dialysis (charging). As the current density increases, more ions are transported during the 120-min charging period, leading to a greater depletion of ions from the dilute solution and a correspondingly higher concentration gradient,  $E_{OCV}$ , and stack resistance (due to the decreased conductivity of the dilute solution).

The calibrated mass-transport model was generally effective in predicting the current and voltage efficiency of the process within experimental uncertainty, as shown in Fig. 6. However, Table 2 shows that the model consistently under-predicted the stack resistance and the  $E_{OCV}$  in the charged state, and the error became more pronounced at higher current densities. At the highest current density, the experimental stack resistance increased nearly six fold to  $11.9 \Omega$ , while the model predicted an increase to only  $4.7 \Omega$ . This discrepancy could be a result of two factors. First, the model does not account for boundary layer effects, but the boundary layer resistance would become increasingly large in comparison to the bulk solution resistance as the dilute solution reaches lower and lower concentrations [40]. Second, Galama et al. have recently shown that the intrinsic membrane resistance increases in proportion to the resistance of the dilute solution when the dilute concentration is below  $0.3 \text{ mol/L}$  [46]. Thus it is possible that the increasingly dilute concentrations reached at the charged state actually increased the intrinsic resistance of the membranes, which this model treats as constant.

#### 4.3. Power density

The average power density delivered during the discharge stage (see Eq. (17)) ranged from  $0.07$  to  $0.44 \text{ W/m}^2$ , with higher power densities associated with higher current densities, as shown in Table 2. While higher maximum power densities have been reported for RED using similar stack configurations [15,43], an energy storage process should not be operated near maximum power density because of the tradeoff relationship with voltage efficiency: at maximum power density, the voltage efficiency cannot exceed 50% [16,47]. However, as a closed loop system, the concentration battery is not limited to naturally-occurring seawater and river water. The use of higher concentrations of electrolyte could both reduce the stack resistance and enable higher concentration gradients to be employed, both of which could increase the average higher power density.

#### 4.4. Energy density

The volumetric energy density of the system was calculated according to Eq. (18). The results were compared to the theoretical Gibbs free energy of mixing calculated according to Eqs. (1)–(3).

Fig. 7 compares the experimental, simulated, and theoretical maximum energy density (with and without activity corrections). The initial state for mixing energy calculations was the fully-charged state (concentration ratios of 2.3:1 – 20:1, as calculated by the model), while the final state was a 2:1 concentration ratio between concentrated and dilute solutions (i.e.  $SOC=33\%$ ), which represents the starting conditions of our charge-discharge experiments (see Table 2). As shown in Fig. 7, the concentration battery recovered between 62% and 77% of the energy theoretically available from the solutions at the fully-charged state. Note that these “energy extraction efficiencies” refer only to the discharge stage. The cyclic energy efficiencies discussed in Section 4.2 were lower because they also account for the energy required to charge the system.

Recent experiments with RED systems have suggested that extraction efficiencies of 45–60% are possible (during the discharge stage) using similar stack conditions to ours when equal volumes of concentrated and dilute solution are used; however, higher efficiencies are obtained when the volume of dilute solution increases relative to that of the concentrated solution [30]. The higher extraction efficiencies reported here are largely due to the fact that the solutions were recirculated in a closed-loop, and therefore, the energy can be harvested during multiple passes of the solutions through the stack

The use of unequal volumes of concentrated and dilute solutions in the closed-loop configuration used in this study may enhance its extraction efficiency further. The fact that the energy extraction efficiency decreases significantly with current density (see Fig. 7) indicates that the inefficiencies are primarily due to ohmic losses rather than osmosis. This is consistent with the fact that during the discharge stage (RED), osmosis and electro-osmosis proceed in opposite directions (see Fig. 2), partially offsetting one another [16,31].

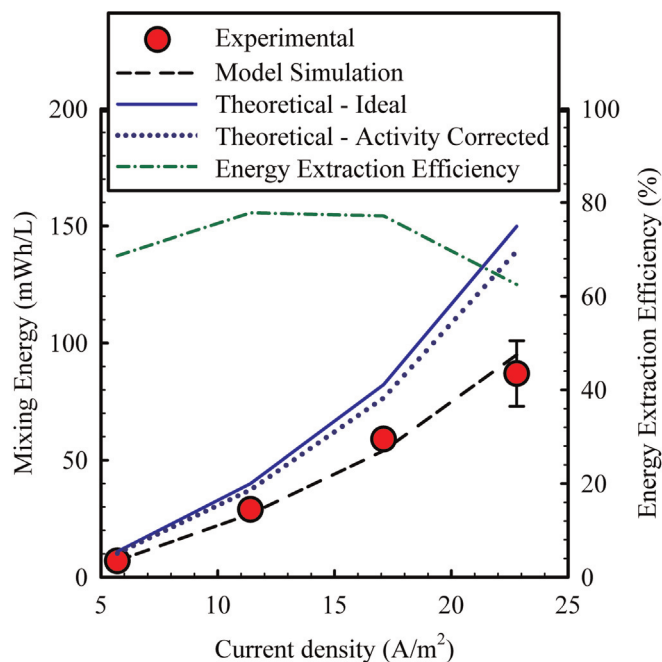


Fig. 7. Experimental, simulated, and theoretical energy density and energy extraction efficiency. Data points and error bars correspond to the average and standard deviation of two replicates, respectively.

#### 4.5. Sources of energy loss

The calibrated engineering model was used to investigate the contribution of the various self-discharge processes to the overall mass flux of salt during the charge–discharge test. In an ideal system, 100% of the flux would result from counter-ion migration and electro-osmosis. In a real system, losses due to osmosis, osmotic convection, co-ion migration, and diffusion reduce the current efficiency of the process. Fig. 8 presents the cumulative total moles of water (Fig. 8A) and ions (Fig. 8B) that were transported through the membrane throughout each charge–discharge test, as calculated by the model. For water, the results indicate that osmosis accounted for more than 75% of the total water flux at low current density, and approximately 50% at higher current density. This difference can be explained by electro-osmosis, the magnitude of which can clearly be seen to increase with current density in Fig. 8A. Regardless of current density, water transport by osmosis was significant, resulting in a net movement of water from the diluted to the concentrated solution over the course of the charge–discharge test. Interestingly, the magnitude of the osmotic water flux also increased with current density, likely as a result of the increased concentration gradients (higher SOC) that were reached at higher current densities; however, the increase in electro-osmosis with current density was much larger.

The model estimates that salt flux was dominated by counter- and co-ion migration, which accounted for between 60% and 85% of total flux (Fig. 8B). The magnitude of the migration flux increased with current density, as expected. Salt diffusion and osmotic convection remained relatively constant at all current densities and each accounted for a roughly equal share of the flux. It is noteworthy that the total flux of water on a molar basis was 30–40 times greater than that of Na<sup>+</sup> and Cl<sup>−</sup> ions, indicating that the transport of water plays a very significant role in energy loss (low current efficiency) compared to diffusion and convection of ions.

#### 4.6. Estimated pumping losses

The model was extended to account for pumping losses by assuming laminar flow [18,43,48] through the solution compartments with an interstitial velocity of 4 cm/s, accounting for the volume occupied by the mesh spacer. The pressure drop under these conditions was calculated as [49]

$$\Delta P = \frac{12\mu Lv}{\epsilon D_h^2}, \quad (31)$$

where  $\mu$  (kg/m s) is the viscosity,  $L$  (m) is the length of the flow path,  $v$  (m/s) is the superficial flow velocity,  $\epsilon$  (–) is the porosity of the spacer, and  $D_h$  (m) is the hydraulic diameter. The pressure drop was converted to energy loss and integrated over the duration of the charge–discharge test. At a current density of 17.1 A/m<sup>2</sup>, pumping losses were estimated to reduce the round-trip energy efficiency from 35.1% to 33.1%. If the average power density produced by the stack during discharging were increased, the impact of the pumping loss would be even less. Alternatively, a lower interstitial velocity could be used to reduce pumping losses, but this may have the undesirable consequence of increasing the boundary layer resistance [13,40]. As with RED systems, there exists an optimum pumping rate that balances increased resistance with hydraulic losses [43].

#### 4.7. Concentration battery performance and directions for optimization

We have discussed the performance of the concentration battery with respect to specific metrics (battery efficiency, power

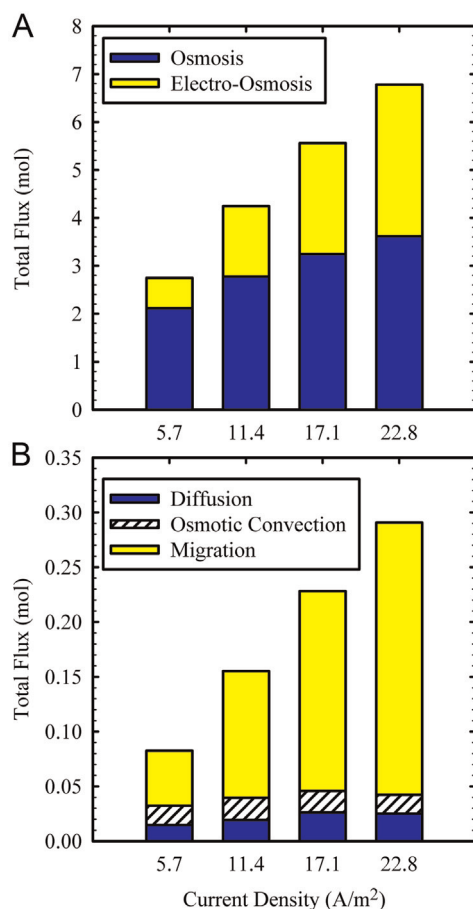


Fig. 8. Relative contribution of mass transport mechanisms to total flux of water (A) H<sub>2</sub>O and (B) NaCl. Mass transport of NaCl represents total moles of both Na<sup>+</sup> and Cl<sup>−</sup> ions.

density, energy density, etc.), but evaluating its potential for practical use requires consideration of multiple factors in combination. For example, batteries for electric cars require both high energy density and high efficiency, while lifetime is less important. For large-scale energy storage (the intended application for the concentration battery), we believe that the most relevant metric is the levelized cost of energy (LCOE) which incorporates information about capital cost, system lifetime, and battery efficiency. This work does not provide enough information to assess the LCOE of the technology as it only investigated the battery efficiency, which itself is inter-related with other parameters such as concentration levels, current density, membrane resistance, etc. However, it is possible to compare certain aspects of the battery performance to more established technologies, and to evaluate directions for further research.

The principal challenge to practical application of the concentration battery is the non-reversibility associated with water transfer by osmosis. A practical battery will require the ability to be charged and discharged thousands of times [3], but our results indicate that osmosis makes it impossible to return the battery to its initial physical state at the end of each cycle. Creative innovations will be required to address this challenge. Optimizations of membrane and electrolyte chemistry may yield some success in slowing the rate of osmosis, but other changes (e.g. replenishment of the dilute solution from an external source) will be needed in order to prevent water transfer completely. Besides enabling long-term operation, reducing or eliminating osmosis will result in a significant increase in the current efficiency, as noted in Section 4.5.

Although the non-optimized round-trip energy efficiencies reported here (21–34%) appear low at first glance (lithium ion batteries for mobile applications can achieve round-trip efficiencies in excess of 99% [35], for example), many technologies considered more suitable for grid-scale deployment (e.g. compressed air energy storage, redox flow and sodium sulfur batteries) only achieve round-trip efficiencies of 60–75% [5], which is consistent with a strategic target of 65% articulated by the U.S. Department of Energy [3]. In some cases, efficiencies as low as 40% could be tolerable if coupled with other desirable system characteristics, such as large capacity or the ability to discharge for many hours or days [3]. As such, with proper optimizations it is feasible that the round-trip energy efficiency of the concentration battery could increase to achieve needed levels for large-scale energy storage.

Power density is not directly comparable to any other battery system due to differences in design; however as with RED for power generation, power density is a major driver of system cost because it determines the amount of membrane that must be used for a given level of power output. The challenge of achieving higher power density is compounded by the fact that an energy storage system should be operated at less-than-maximum power density in order to preserve the energy efficiency (see Section 4.3). Therefore, optimizations of membrane, electrolyte chemistry, and stack design that enable higher power density from RED stacks will be directly applicable to (R)ED energy storage systems as well.

The volumetric energy density of the electrolyte solutions will ultimately dictate the physical size of a practical concentration battery system. The energy densities achieved in this first attempt (approximately 0.05 Wh/L) are many times lower than the energy density of typical batteries for stationary applications (e.g. 16–33 Wh/L for vanadium redox flow batteries [50]). However, significant increases could be made by employing more concentrated electrolyte solutions. For example, according to Eqs. (1)–(3), a system in which concentrated and dilute solutions of 5m and 0.5m NaCl represented the fully charged state that is discharged to 33% SOC could yield more than 1.3 Wh/L, more than an order of magnitude greater than the highest energy density measured in this work. Other high-solubility electrolytes could further enhance the energy density, but at present, the use of such high concentrations is not practical due to energy losses associated with high rates of osmosis as described in Section 4.5. Custom-tailored membranes with low resistance and more effective control of osmosis could increase the energy extraction efficiency, allowing more of the available mixing energy to be captured and thus improving the energy density further.

Even with these improvements, the theoretically-available energy density of such electrolyte solutions would still be lower than that of redox flow batteries. However, despite its relatively low energy density, the low-cost and non-toxic nature of electrolytes such as sodium chloride could make the concentration battery attractive for certain stationary applications in which space constraints are not significant (e.g. a large-scale solar or wind farm in a rural area). The ability of this system to store very large amounts of energy (limited only by the volume of the electrolyte solutions) is another attribute that distinguishes the concentration battery from many other energy storage technologies.

Given the numerous inter-dependencies between membrane properties, electrolyte chemistry, and system performance characteristics, a complete techno-economic analysis of the concentration battery for the application of grid-scale energy storage will be required before specific performance targets (e.g. membrane resistance or electrolyte energy density) for commercial application can be defined.

## 5. Conclusions

In this paper we presented a new method of energy storage using salinity gradients and a corresponding rechargeable battery based on closed-loop electro dialysis. We formulated a mass transport model based on chemical thermodynamic theory that describes the performance of the battery. We showed experimental round-trip energy efficiency, power density, and energy density of the battery and compared the results to the predictions of the model. The following points highlight the main aspects of our findings:

- This first attempt to use electro dialytic processes for reversible energy storage demonstrates that a functioning battery can be constructed using typical RED stack components and commercially available ion exchange membranes.
- The experimental energy extraction efficiency from the solutions was relatively high (i.e. between 62% and 77% of the theoretical Gibbs energy change) in large part due to the fact that the battery was a closed-loop system.
- An engineering model based on chemical thermodynamics and RED process predicted the current efficiency within experimental error at all current efficiencies studied, while the predicted voltage efficiency was slightly outside of experimental error. This discrepancy is attributed to boundary layer resistance not accounted for in the model.
- Round-trip energy efficiency varied from 21% to 34% over a range of current densities, and exhibited the expected tradeoffs between ohmic losses and faradaic losses, with high current efficiency (i.e. 58.9%) at high current density, and high voltage efficiency (i.e. 78.5%) at low current density.
- Model results suggest that osmosis is the dominant source of faradaic losses, while salt diffusion through the membranes appears to be less important. By causing non-reversible water transfer between the two electrolyte compartments, osmosis prevents returning the battery to its initial physical state after charging and discharging.
- The average power densities extracted by the device are somewhat lower than power densities reported for RED due to our focus on maximizing battery efficiency.
- Future improvements in membrane technology and optimization of the system chemistry are necessary to improve the power density, energy density, and round-trip energy efficiency of the process.
- The use of low-cost electrolytes and the ability to independently scale power capacity (i.e. membrane area) and energy capacity (i.e. electrolyte volume) could make this technology well-suited for applications where low volumetric energy density may be tolerable, such as large-scale wind or solar power arrays located in rural areas.

Research in RED to date has focused primarily on maximizing the power density for continuous power generation (e.g. from sea and river water). The data presented here suggest additional design objectives (e.g. battery efficiency, energy density) for optimization of RED technology in the new application of energy storage. Future research should focus on tailoring the membrane-electrolyte system to achieve the most cost-effective balance between these three performance metrics.

## Funding sources

This work was funded by Bluecell Energy LLC. Dr. Orlando Coronell was supported by the National Science Foundation (NSF) Grant Opportunities for Academic Liaison with Industry (GOALI)

and Chemical and Biological Separations programs under Award#1264690, and NSF Environmental Engineering program under Award#1336532. FuMA-Tech GmbH provided the ion exchange membranes.

## Acknowledgment

The authors would like to thank Dr. Igor Kadija (ECSI Fibrottools; Raleigh, NC) for his assistance in developing laboratory techniques and troubleshooting the apparatus. We are also grateful to Kelly D. Boone (Bluecell Energy) and Dr. Nicholas DeFelice (Columbia University) for helpful discussions concerning the energy storage market and the mass transport calculations, respectively.

## Appendix A. Supplementary information

Supplementary data associated with this article can be found in the online version at <http://dx.doi.org/10.1016/j.memsci.2015.06.050>.

### Nomenclature

#### List of symbols

$a$	activity (–)
$A$	open membrane area (m <sup>2</sup> )
$C$	molar concentration (mol/L)
$D$	diffusion coefficient (m <sup>2</sup> /s)
$D_h$	hydraulic diameter (m)
$E$	battery voltage (V)
$F$	Faraday constant (96,485 C/mol)
$G$	Gibbs energy (J)
$I$	current (A)
$j$	current density (A/m <sup>2</sup> )
$J$	flux (mol/m <sup>2</sup> s)
$K_{ff}$	membrane form factor (–)
$L$	flow path length (m)
$m$	concentration (mol/kg)
$n$	number of moles (mol)
$N$	number of membrane pairs (–)
$P$	pressure (Pa)
$r$	membrane area resistance (Ω m <sup>2</sup> )
$R$	ideal gas constant (8.314 J/mol K) or resistance (Ω)
$t_c, t_d$	charging or discharging time (s)
$t_i, t_w$	transport number (mol substance/mol charge)
$T$	temperature (K)
$v$	flow velocity (m/s)
$V$	Volume (m <sup>3</sup> )
$V^m$	Molar volume (m <sup>3</sup> /mol)
$x$	membrane thickness (m)
$x_i$	mole fraction (–)
$X$	membrane fixed charge density (eq/L)
$z$	charge (eq)

#### Greek letters

$\alpha$	membrane permselectivity (–)
$\beta$	spacer shadow factor (–)
$\gamma$	activity coefficient (kg/mol)
$\delta$	thickness (m)
$\Delta$	change between two positions or states
$\epsilon$	spacer porosity (–)

$\kappa$	conductivity (S/m)
$\eta$	round-trip energy efficiency (–)
$\mu$	absolute viscosity (kg/m s)
$\mu_k$	kinematic viscosity (m <sup>2</sup> /s)
$\pi$	osmotic pressure (Pa)
$\psi$	electric potential (V)
$\nu$	stoichiometric coefficient (–)

#### Subscripts and decorations

overbar	membrane phase
–	anion in the salt
+	cation in the salt
$c$	charging stage
$C$	concentrated solution
$d$	discharging stage
$D$	dilute solution
$i$	chemical species $i$
$I$	current (efficiency)
$V$	voltage (efficiency)
$w$	water
$AEM$	anion exchange membrane
$CEM$	cation exchange membrane
$OCV$	open circuit voltage

## References

- [1] S. Wilkinson, A. Ward, The Future of Grid-Connected Energy Storage: An Analysis of the Business Case and Market Potential – 2014 Edition (2014).
- [2] A.A. Akhil, G. Huff, A.B. Currier, B.C. Kaun, D.M. Rastler, S.B. Chen, et al., DOE/EPRI 2013 Electricity Storage Handbook in Collaboration with NRECA (2013).
- [3] U.S. Department of Energy, Grid Energy Storage (2013).
- [4] K. Bradbury, L. Pratson, D. Patiño-Echeverri, Economic viability of energy storage systems based on price arbitrage potential in real-time U.S. electricity markets, *Appl. Energy* 114 (2014) 512–519, <http://dx.doi.org/10.1016/j.apenergy.2013.10.010>.
- [5] B. Dunn, H. Kamath, J.-M. Tarascon, Electrical energy storage for the grid: a battery of choices, *Science* 334 (2011) 928–935, <http://dx.doi.org/10.1126/science.1212741>.
- [6] *Water Treatment Membrane Processes*, in: J. Mallevalle, P.E. Odendaal, M. R. Wiesner (Eds.), McGraw-Hill, US, 1996.
- [7] *Ion Exchange Membranes: Fundamentals and Applications*, in: Y. Tanaka (Ed.), Elsevier, Amsterdam, The Netherlands, 2007.
- [8] J.N. Weinstein, F.B. Leitz, Electric power from differences in salinity: the dialytic battery, *Science* 191 (1976) 557.
- [9] J.W. Post, H.V.M. Hamelers, C.J.N. Buisman, Energy recovery from controlled mixing salt and fresh water with a reverse electrodialysis system, *Environ. Sci. Technol.* 42 (2008) 5785–5790.
- [10] J.W. Post, J. Veerman, H.V.M. Hamelers, G.J.W. Euverink, S.J. Metz, K. Nijmeijer, et al., Salinity-gradient power: evaluation of pressure-retarded osmosis and reverse electrodialysis, *J. Membr. Sci.* 288 (2007) 218–230, <http://dx.doi.org/10.1016/j.memsci.2006.11.018>.
- [11] J. Veerman, M. Saakes, S.J. Metz, G.J. Harmsen, Electrical power from sea and river water by reverse electrodialysis: a first step from the laboratory to a real power plant, *Environ. Sci. Technol.* 44 (2010) 9207–9212.
- [12] J. Veerman, M. Saakes, S.J. Metz, G.J. Harmsen, Reverse electrodialysis: performance of a stack with 50 cells on the mixing of sea and river water, *J. Membr. Sci.* 327 (2009) 136–144, <http://dx.doi.org/10.1016/j.memsci.2008.11.015>.
- [13] P. Długolecki, A. Gambier, K. Nijmeijer, M. Wessling, Practical potential of reverse electrodialysis as process for sustainable energy generation, *Environ. Sci. Technol.* 43 (2009) 6888–6894.
- [14] D.A. Vermaas, D. Kunteng, M. Saakes, K. Nijmeijer, Fouling in reverse electrodialysis under natural conditions, *Water Res.* 47 (2013) 1289–1298, <http://dx.doi.org/10.1016/j.watres.2012.11.053>.
- [15] A. Daniilidis, D.A. Vermaas, R. Herber, K. Nijmeijer, Experimentally obtainable energy from mixing river water, seawater or brines with reverse electrodialysis, *Renew. Energy* 64 (2014) 123–131, <http://dx.doi.org/10.1016/j.renene.2013.11.001>.
- [16] J. Veerman, R.M. de Jong, M. Saakes, S.J. Metz, G.J. Harmsen, Reverse electrodialysis: comparison of six commercial membrane pairs on the thermodynamic efficiency and power density, *J. Membr. Sci.* 343 (2009) 7–15, <http://dx.doi.org/10.1016/j.memsci.2009.05.047>.

- [17] N.Y. Yip, D.A. Vermaas, K. Nijmeijer, M. Elimelech, Thermodynamic, energy efficiency, and power density analysis of reverse electro dialysis power generation with natural salinity gradients, *Environ. Sci. Technol.* 48 (2014) 4925–4936, <http://dx.doi.org/10.1021/es5005413>.
- [18] E. Brauns, Finite elements-based 2D theoretical analysis of the effect of IEX membrane thickness and salt solution residence time on the ion transport within a salinity gradient power reverse electro dialysis half cell pair, *Desalination Water Treat.* 51 (2013) 6429–6443, <http://dx.doi.org/10.1080/19443994.2013.807905>.
- [19] E. Güler, W. van Baak, M. Saakes, K. Nijmeijer, Monovalent-ion-selective membranes for reverse electro dialysis, *J. Membr. Sci.* 455 (2014) 254–270, <http://dx.doi.org/10.1016/j.memsci.2013.12.054>.
- [20] E. Güler, R. Elizen, D.A. Vermaas, M. Saakes, K. Nijmeijer, Performance-determining membrane properties in reverse electro dialysis, *J. Membr. Sci.* 446 (2013) 266–276, <http://dx.doi.org/10.1016/j.memsci.2013.06.045>.
- [21] P. Długolecki, K. Nijmeijer, S.J. Metz, M. Wessling, Current status of ion exchange membranes for power generation from salinity gradients, *J. Membr. Sci.* 319 (2008) 214–222, <http://dx.doi.org/10.1016/j.memsci.2008.03.037>.
- [22] E. Güler, Y. Zhang, M. Saakes, K. Nijmeijer, Tailor-made anion-exchange membranes for salinity gradient power generation using reverse electro dialysis, *ChemSusChem* 5 (2012) 2262–2270, <http://dx.doi.org/10.1002/cssc.201200298>.
- [23] J. Veerman, M. Saakes, S.J. Metz, G.J. Harmsen, Reverse electro dialysis: evaluation of suitable electrode systems, *J. Appl. Electrochem.* 40 (2010) 1461–1474, <http://dx.doi.org/10.1007/s10800-010-0124-8>.
- [24] O. Scialdone, C. Guarisco, S. Grispo, A. D'Angelo, A. Galia, Investigation of electrode material – redox couple systems for reverse electro dialysis processes. Part I: iron redox couples, *J. Electroanal. Chem.* 681 (2012) 66–75, <http://dx.doi.org/10.1016/j.jelechem.2012.05.017>.
- [25] O. Scialdone, A. Albanese, A. D'Angelo, A. Galia, C. Guarisco, Investigation of electrode material – redox couple systems for reverse electro dialysis processes. Part II: experiments in a stack with 10–50 cell pairs, *J. Electroanal. Chem.* 704 (2013) 1–9, <http://dx.doi.org/10.1016/j.jelechem.2013.06.001>.
- [26] G.M. Geise, M. a Hickner, B.E. Logan, Ammonium bicarbonate transport in anion exchange membranes for salinity gradient energy, *ACS Macro Lett.* 2 (2013) 814–817, <http://dx.doi.org/10.1021/mz4003408>.
- [27] X. Luo, X. Cao, Y. Mo, K. Xiao, X. Zhang, P. Liang, et al., Power generation by coupling reverse electro dialysis and ammonium bicarbonate: implication for recovery of waste heat, *Electrochem. Commun.* 19 (2012) 25–28, <http://dx.doi.org/10.1016/j.elecom.2012.03.004>.
- [28] M.C. Hatzell, I. Ivanov, R.D. Cusick, X. Zhu, B.E. Logan, Comparison of hydrogen production and electrical power generation for energy capture in closed-loop ammonium bicarbonate reverse electro dialysis systems, *Phys. Chem. Chem. Phys.* 16 (2014) 1632–1638, <http://dx.doi.org/10.1039/c3cp54351j>.
- [29] Y. Koga, *Solution Thermodynamics and Its Application to Aqueous Solutions: A Differential Approach*, 1st ed., Elsevier B.V., Amsterdam, 2007.
- [30] D.A. Vermaas, J. Veerman, N.Y. Yip, M. Elimelech, M. Saakes, K. Nijmeijer, High efficiency in energy generation from salinity gradients with reverse electro dialysis, *ACS Sustain. Chem. Eng.* 1 (2013) 1295–1302.
- [31] G.M. Geise, H.J. Cassidy, D.R. Paul, E. Logan, M.A. Hickner, Specific ion effects on membrane potential and the permselectivity of ion exchange membranes, *Phys. Chem. Chem. Phys.* 16 (2014) 21673–21681, <http://dx.doi.org/10.1039/C4CP03076A>.
- [32] T. Sata, *Ion Exchange Membranes: Preparation, Characterization, Modification, and Application*, Royal Society of Chemistry, Cambridge, UK, 2004.
- [33] H. Strathmann, *Ion Exchange Membrane Separation Processes*, Elsevier, Amsterdam, The Netherlands, 2004.
- [34] J.O. Bockris, A.K.N. Reddy, *Modern Electrochemistry*, Plenum Press, New York, NY, 1977.
- [35] R. Lu, A. Yang, Y. Xue, L. Xu, C. Zhu, Analysis of the key factors affecting the energy efficiency of batteries in electric vehicle, *World Electr. Veh. J.* 4 (2010) 9–13.
- [36] C. Larchet, B. Auclair, V. Nikonenko, Approximate evaluation of water transport number in ion-exchange membranes, *Electrochim. Acta* 49 (2004) 1711–1717, <http://dx.doi.org/10.1016/j.electacta.2003.11.030>.
- [37] K. Kontturi, L. Murtomäki, J.A. Manzanares, Donnan Equilibrium in Charged Membranes, in: *Ion. Transp. Process. Electrochem. Membr. Sci.*, Oxford University Press (2008) pp. 152–166.
- [38] P.M. May, D. Rowland, G. Hefter, E. Königsberger, A generic and updatable pitzer characterization of aqueous binary electrolyte solutions at 1 bar and 25 °C, *J. Chem. Eng. Data* 56 (2011) 5066–5077, <http://dx.doi.org/10.1021/jc2009329>.
- [39] V.K. Shahi, A.P. Murugesu, B.S. Makwana, S.K. Thampy, R. Rangarajan, Comparative investigations on the electrical conductance of ion-exchange membranes, *Indian J. Chem.* 39A (2000) 1264–1269.
- [40] P. Długolecki, P. Ogonowski, S.S.J. Metz, et al., On the resistances of membrane, diffusion boundary layer and double layer in ion exchange membrane transport, *J. Membr. Sci.* 349 (2010) 369–379, <http://dx.doi.org/10.1016/j.memsci.2009.11.069>.
- [41] G.M. Geise, M.A. Hickner, B.E. Logan, Ionic resistance and permselectivity tradeoffs in anion exchange membranes, *ACS Appl. Mater. Interfaces* 5 (2013) 10294–10301, <http://dx.doi.org/10.1021/am403207w>.
- [42] J.F. Whitacre, T. Wiley, S. Shanbhag, Y. Wenzhuo, A. Mohamed, S.E. Chun, et al., An aqueous electrolyte, sodium ion functional, large format energy storage device for stationary applications, *J. Power Sources* 213 (2012) 255–264, <http://dx.doi.org/10.1016/j.jpowsour.2012.04.018>.
- [43] D.A. Vermaas, M. Saakes, K. Nijmeijer, Doubled power density from salinity gradients at reduced intermembrane distance, *Environ. Sci. Technol.* 45 (2011) 7089–7095.
- [44] FuMA-Tech GmbH, Technical Data Sheet – Fumasep FKE-20 (2014).
- [45] FuMA-Tech GmbH, Technical Data Sheet – Fumasep FAS-20 (2014).
- [46] A.H. Galama, D.A. Vermaas, J. Veerman, M. Saakes, H.H.M. Rijnaarts, J.W. Post, et al., Membrane resistance: the effect of salinity gradients over a cation exchange membrane, *J. Membr. Sci.* 467 (2014) 279–291, <http://dx.doi.org/10.1016/j.memsci.2014.05.046>.
- [47] J. Veerman, J.W. Post, M. Saakes, S.J. Metz, G.J. Harmsen, Reducing power losses caused by ionic shortcut currents in reverse electro dialysis stacks by a validated model, *J. Membr. Sci.* 310 (2008) 418–430, <http://dx.doi.org/10.1016/j.memsci.2007.11.032>.
- [48] J. Veerman, M. Saakes, S.J. Metz, G.J. Harmsen, Reverse electro dialysis: a validated process model for design and optimization, *Chem. Eng. J.* 166 (2011) 256–268, <http://dx.doi.org/10.1016/j.cej.2010.10.071>.
- [49] D.A. Vermaas, M. Saakes, K. Nijmeijer, Early detection of preferential channeling in reverse electro dialysis, *Electrochim. Acta* 117 (2014) 9–17, <http://dx.doi.org/10.1016/j.electacta.2013.11.094>.
- [50] Chen Haisheng, Thang Ngoc Cong, Yang Wei, Tan Chunqing, Li Yongliang, Ding Yulong, Progress in electrical energy storage system: a critical review, *Prog. Nat. Sci.* 19 (2009) 291–312, <http://dx.doi.org/10.1016/j.pnsc.2008.07.014>.